Electronic Supplementary Material (ESI) for Journal of Materials Chemistry A.
This journal is © The Royal Society of Chemistry 2019

Supporting Information

On Understanding Bandgap Bowing and Optoelectronic Quality in Pb-Sn Alloy Hybrid Perovskites

Adharsh Rajagopal,[1] *Ryan J. Stoddard,*[2] *Hugh W. Hillhouse,*[2*] *and Alex K.-Y. Jen*[1,3,4*]

[1]Department of Materials Science and Engineering, University of Washington, Seattle, WA, 98195-2120, USA

[2]Department of Chemical Engineering, Molecular Engineering and Sciences Institute, University of Washington, Seattle, WA 98195-1750, USA

[3]Department of Materials Science & Engineering, City University of Hong Kong, Kowloon, Hong Kong

[4]Department of Chemistry, City University of Hong Kong, Kowloon, Hong Kong

[*]Corresponding Author. E-mail: h2@uw.edu, ajen@uw.edu

Experimental Section

Materials: Soda lime glass substrate was purchased from Colorado Concept Coatings LLC. CsI, PbI_2, $PbBr_2$, SnI_2 (99.999% trace metal basis), SnF_2 (99%) and all anhydrous solvents (DMF, DMSO, Toluene) used in this work were purchased from Sigma-Aldrich. $SnBr_2$ (Alfa Aesar, 99.4%) was purchased from Fisher Scientific. Organic salts (MAI, MABr, FAI, GAI) were purchased from Greatcell Solar.

Perovskite solution preparation: AMX_3 perovskite precursor solutions were prepared by adding 1 M 1:1 AX:MX_2 salts in 0.5 ml of 7:3 DMF:DMSO co-solvent system; additionally 10 mol% SnF_2 was included in $ASnX_3$ solutions (**Table S1a**). Precursors were dissolved by stirring the solutions at 70 °C for 2 h. All solutions were stored at room temperature overnight before use. Solutions for perovskite compositions with multiple *A*-site and *B-site* cations were obtained by mixing the end member AMX_3 solutions (maintained at room temperature) in appropriate ratios according to the stoichiometry (**Tables S1b-c**). All solutions were mixed well, left at room temperature and used without further filtering before spin coating.

Perovskite film fabrication: Glass substrates were cleaned using sequential steps of ultrasonication for 10 min in detergent, deionized water, acetone, and isopropanol alcohol. Cleaned glass substrates were subjected to UV ozone treatment (10 min) before film fabrication. Perovskite precursor solution was spin coated onto the substrate using 2-step spin program (1000 rpm for 5 s , 5000 rpm for 30 s); during the last 20-15 s of the second spin-coating step, toluene (0.7 ml) was dropped onto the spinning substrate. Substrates were then annealed for 15 min at 100 ^oC (for films with MA, MACs and MAGA as *A*-site), 160 ^oC (for films with FA, FACs and MAFA as *A*-site) and 350 ^oC (for films with pure Cs as *A*-site) using a hot plate. Solution handing and film fabrication were carried out inside a glovebox (H_2O and O_2 levels ~ 0.1 – 10 ppm).

Bandgap measurement and analysis: Thin film absorption measurements were carried out using Varian Cary 5000 UV-Vis-NIR spectrometer. Bandgap values were estimated from the absorption spectrum onset extracted using the 'steepest gradient' method, in accordance to the recommendation by Parrott et al.[1] In their work, they find that 'Steepest gradient' method is more reliable than 'Tauc Plot method' for comparison of absorption onsets in Pb-Sn perovskite alloys. 'Steepest Gradient' method cannot be used to accurately determine the true band-gap, but rather provides more meaningful results for quantitatively comparing the absorption onsets because of its less sensitivity to problems commonly encountered with 'Tauc Plot' method. It is important to note that bandgap values obtained using 'Steepest Gradient' method is larger than values from 'Tauc Plot' method (example in **Figure S13b**). We use this internally consistent method to compare bandgap values for different compositions and use them in the bandgap bowing analysis (**Figures 1-3** and **S6**). We use 'Tauc Plot' method when we need an accurate estimation of the bandgap value and to compare them in perspective with values reported in literature.

Bandgap bowing parameter (b) is obtained using quadratic fit of the bandgap data as a function of composition for a given series of Pb-Sn or I-Br alloy:

$$y(x) = E_g(I_{1-x}II_x) = (1-x).E_g(I) + (x).E_g(II) - b.(x).(1-x) \quad \text{or} \quad y(x) = E_g(I_{1-x}II_x) = ax + bx^2 + c$$

where, $a = [(E_g(II) - E_g(I) - b]$ and $c = E_g(I)$.

Adjusted R^2 values estimate the goodness of the fits (**Tables S3**, **S8** and **S9**). Bowing analysis is sensitive to the bandgap values and hence the choice of method used for bandgap determination must be taken into consideration for comparison with values in literature. With same analysis method, bandgap values and bowing parameter for $FAPb_{1-x}Sn_xI_3$ in our work match well with that reported by Parrott et al.[1]

X-ray diffraction and strain analysis: A Bruker D8 Discover Microfocus XRD with a Cu Kα source and 1D detector was used for XRD measurements to achieve a higher resolution and accurately determine broadening parameters. Similar to our previous works,[2,3] we use powder samples (scrapped from thin film samples) for attaining better sampling distribution and get diffraction signal from additional planes compared to thin films which often show signal from limited set of planes because of preferential orientation; peak positions were unchanged in powder and thin film samples. All XRD peaks were indexed manually and used for determining the lattice parameters. The evolutionary algorithm in the Solver package of Excel was used to minimize the sum of residuals squared produced between measured and calculated plane spacings to arrive at lattice parameters providing the best fit for the data assuming either tetragonal or cubic Bravais lattice.[4] Tetragonal system lattice parameters (a and c) were converted to pseudo-cubic lattice parameters based on the geometric relationship between them: $a^* = \frac{\sqrt{2a^2}}{2}; c^* = \frac{c}{2}$ and the average of a^* and c^* was used to determine a single pseudo-cubic lattice parameter.[5]

Broadening values for XRD peaks (Δd_{hkl}) and instrumental broadening (Δd_{ins}) were determined using MDI JADE (an XRD pattern processing software); Pearson-VII peak shape function provided the best fit for all samples in this work. Microstrain (ε) values were obtained using a modified Williamson-Hall (W-H) analysis method:[6] $\Delta d_{hkl}^2 - \Delta d_{ins}^2 = \Delta d_{size}^2 + \varepsilon^2 d^2$. Accordingly, $(\Delta d_{hkl}^2 - \Delta d_{ins}^2)^{0.5}$ was plotted versus d and the slope of the linear fit gives ε (**Figures S4** and **S7**). We found this method of analysis is more suited for samples with anisotropic strain and has also been applied in previous perovskite works.[7,8] We used only {hk0} peaks for linear fits in samples with tetragonal crystal structure,[9] whereas all {hkl} peaks were used for linear fits in samples with cubic crystal structure. Adjusted R^2 values in **Figures S4b** and **S7b** estimate the goodness of the fits.

Composition exploration via spray coating: Spray coated experiments were conducted with a similar methodology as described previously.[3] In this study, we employed an anti-solvent bath approach to control perovskite crystallization in order to attain the most relevant comparison with spin coated films. Stoichiometric perovskite inks were prepared at 0.25 M concentration in 80/20 vol/vol DMF/DMSO and stirred. 10 mol% SnF_2 relative to Sn content was also included in each ink. Perovskite ink was deposited in a N_2-filled glovebox via an ultrasonic spray nozzle, which translated above the substrate, delivering ink at a constant rate of 100 µL/min while translating along the 75mm x 25mm glass substrate at a rate of 1 mm/s. A composition gradient was achieved by mixing streams delivered by two pumps with linearly changing flow rates, one ramping up and one ramping down such that 100 µL/min total flow rate was maintained. After ink deposition, the substrate was left to dry for 1 minute (at room temperature), then submerged in a diethyl ether bath for 1 minute or until the color stopped changing. Then the substrate was annealed at 160 ˚C for 10 minutes.

Although the syringe pumps are ramped in a linearly from the two end member solutions, the gradient on the substrate will not be precisely linear due to mixing effects. Since it is difficult to measure changes in organic cation ratios, we fabricated a pure Pb to pure Sn gradient to validate our process, and quantified the Pb-Sn ratio with Energy Dispersive Spectroscopy (EDS), as shown in **Figure S10a**. This "Composition Gradient Function" was used to infer composition for other gradients.

Photoluminescence (PL) measurements: Confocal absolute intensity PL was performed as reported previously.[10] Samples were excited with a 532nm laser and calibrated to above bandgap photon flux (1 Sun, 10 Suns, or 100 Suns) (for a 1.2eV bandgap material based on AM1.5GT spectrum) using an Oriel optical power meter and beam profiler. Photoluminescence spectra were collected with a Horiba LabRAM HR-800 with 10x objective using a monochromator blazed at 1200mm with 150 gr/mm with confocal hole set to 800 µm. Calibration of the photon detection rate was performed with a blackbody source (IR-301, Infrared Systems Development) at 1050 ˚C with a pinhole size of 10 µm to determine a calibration factor for photons per count for this system.

For spin coated films, PL measurements were collected at 1 Sun, 10 Suns, and 100 Suns with both a Si and InGaAs detector (as emission of ~1.2 eV lies in a non-ideal range for either detector). We found minimal dependence of PLQY on illumination intensity, and the 100 Suns measurements gave best signal-to-noise for all samples. PL Peak position was determined by taking the PL peak maximum after conversion to absolute intensity units. Quasi-Fermi Level splitting was determined using the PLQY method, first proposed by Ross:[11]

$$\Delta E_F = \Delta E_{F,max} + kT \ln PLQY_{Ext}$$

In this work, we used the 1 Sun Shockley-Queisser limit (assuming the bandgap equals the PL peak position) for $\Delta E_{F,max}$, we assumed T = 300K, and we used PLQY determined from 100 Sun measurement (see **Figure S14** for 1 Sun and 100 Sun comparison).

Statistics for spin coated films were collected by taking 25 measurements spatially distributed across the substrate with illumination times of 1-5 s each. Statistics for spray coated films were collected in a grid of 10 measurements along the width and 36 measurements along the length of the gradient. The statistics of each set of 10 lateral measurements were averaged to create a series of 36 data points describing the characteristics along the length of the gradient (**Figures S10b-c** show one example gradient). The response surfaces shown in ternary plots were created by fitting a polynomial model to interpolate within all the spray coating data.

The above “PLQY method” for quasi-Fermi level splitting determination does not account for deviations in the peak position from true bandgap nor does it consider losses due to sub-bandgap absorptivity. We employed the “full peak fit” method first derived by Katahara and Hillhouse,[12] where the photoluminescence is fit to a modified Lasher-Stern-Wuerfel equation given by:

$$I_{PL}(E) = \frac{2\pi E^2}{h^3 c^2} \cdot \frac{a(E, \Delta E_F, T)}{\exp\left(\frac{E - \Delta E_F}{kT}\right) - 1}$$

Details about the absorption model used can be found in the publication by Katahara and Hillhouse.[12] The data in **Figure 4f** was measured at ~100 Suns then corrected to 1 Suns using an Oriel optical power to quantify excitation intensity. **Figure S14** demonstrates the validity of this approach.

Additional Discussion of Spray Coating Results

Spray coated results for the FAGACs dataset are shown in **Figure S11**. We observe that adding GA will blue shift the bandgap and give a slight increase in optoelectronic properties, with the maximum $\mathcal{X}$ occurring at A = $FA_{0.42}Cs_{0.45}GA_{0.12}$. We note comparable A = (FA,Cs) binary compositions have slightly lower $\mathcal{X}$ than the same compositions in the (FA,MA,Cs) dataset, which likely arises due to differences in quantities of Sn^{2+} oxidation.

Supplementary Tables

Table S1a. Quantity of precursors for making solutions of end member (AMX_3) compositions.

AMX_3 **Composition**	AX **salt**	MX_2 **salt**	**Additive**	**Solvent**	
$MAPbI_3$	MAI (mg)	PbI_2 (mg)		DMF (μl)	DMSO (μl)
	79.5	230.5		350	150
$MASnI_3$	MAI (mg)	SnI_2 (mg)	SnF_2 (mg)	DMF (μl)	DMSO (μl)
	79.5	186.3	7.8	350	150
$FAPbI_3$	FAI (mg)	PbI_2 (mg)		DMF (μl)	DMSO (μl)
	86.0	230.5		350	150
$FASnI_3$	FAI (mg)	SnI_2 (mg)	SnF_2 (mg)	DMF (μl)	DMSO (μl)
	86.0	186.3	7.8	350	150
$CsPbI_3$	CsI (mg)	PbI_2 (mg)		DMF (μl)	DMSO (μl)
	129.9	230.5		350	150
$CsSnI_3$	CsI (mg)	SnI_2 (mg)	SnF_2 (mg)	DMF (μl)	DMSO (μl)
	129.9	186.3	7.8	350	150
$GAPbI_3$	GAI (mg)	PbI_2 (mg)		DMF (μl)	DMSO (μl)
	93.5	230.5		350	150
$GASnI_3$	GAI (mg)	SnI_2 (mg)	SnF_2 (mg)	DMF (μl)	DMSO (μl)
	93.5	186.3	7.8	350	150
$MAPbBr_3$	MABr (mg)	$PbBr_2$ (mg)		DMF (μl)	DMSO (μl)
	56.0	183.5		350	150
$MASnBr_3$	MABr (mg)	$SnBr_2$ (mg)	SnF_2 (mg)	DMF (μl)	DMSO (μl)
	56.0	139.3	7.8	350	150

Table S1b. Quantity of end member solutions mixed to get precursor solutions for compositions with mixed *A*-site.

AMI_3 **solutions,** M **= Pb or Sn (for 100 μl)**					
Notation	A-site	$MAMI_3$ (μl)	$FAMI_3$ (μl)	$CsMI_3$ (μl)	$GAMI_3$ (μl)
MACs	$MA_{0.8}Cs_{0.2}$	80	-	20	-
MAGA	$MA_{0.8}GA_{0.2}$	80	-	-	20
FACs	$FA_{0.8}Cs_{0.2}$	-	80	20	-
MAFA	$MA_{0.5}FA_{0.5}$	50	50	-	-
MAFACs	$MA_{0.24}FA_{0.61}Cs_{0.15}$	24	61	15	-
FAGACs	$FA_{0.42}GA_{0.12}Cs_{0.46}$	-	42	46	12

Table S1c. Quantity of end member solutions mixed to get $A\mathrm{Pb}_{1-x}\mathrm{Sn}_xX_3$ precursor solutions.

$A\mathrm{Pb}_{1-x}\mathrm{Sn}_xX_3$ solutions (for 100 µl)			
Notation	x	$A\mathrm{Pb}X_3$ (µl)	$A\mathrm{Sn}X_3$ (µl)
Pb	0.00	100	0
25Sn	0.25	75	25
50Sn	0.50	50	50
75Sn	0.75	25	75
Sn	1.00	0	100

Table S2. Crystal structure and lattice parameters for $\mathrm{MAPb}_{1-x}\mathrm{Sn}_x\mathrm{I}_3$ ($0 \leq x \leq 1$) alloys.

Composition	**Crystal Structure**	**Lattice Parameters**		
		Tetragonal		**Pseudo-cubic**
		a = b (Å)	c (Å)	(Å)
MAPbI_3	Tetragonal	8.88	12.67	6.306
$\mathrm{MAPb}_{0.75}\mathrm{Sn}_{0.25}\mathrm{I}_3$	Tetragonal	8.87	12.61	6.289
$\mathrm{MAPb}_{0.50}\mathrm{Sn}_{0.50}\mathrm{I}_3$	(Pseudo)Cubic	-	-	6.268
$\mathrm{MAPb}_{0.25}\mathrm{Sn}_{0.75}\mathrm{I}_3$	(Pseudo)Cubic	-	-	6.259
MASnI_3	(Pseudo)Cubic	-	-	6.249

Table S3. Quadratic fit parameters for composition dependence of bandgap in $A\mathrm{Pb}_{1-x}\mathrm{Sn}_xX_3$ alloys.

Bowing (b) in $A\mathrm{Pb}_{1-x}\mathrm{Sn}_xX_3$ alloys obtained from quadratic fit of E_g data: **$y = E_g(x) = ax + bx^2 + c$**						
A-site	X-site	a (E_{Sn} - E_{Pb} - b)	**b, eV**	c (E_{pb})	Adjusted R^2	Location of $E_{g,\ min}$ (x_{min})
Cs	I	-0.98	**0.57 ± 0.06**	1.76	0.993	0.86
MA	I	-0.95	**0.61 ± 0.03**	1.62	0.998	0.78
FA	I	-0.89	**0.77 ± 0.06**	1.55	0.983	0.58
$\mathrm{FA}_{0.8}\mathrm{Cs}_{0.2}$	I	-0.96	**0.75 ± 0.07**	1.58	0.981	0.64
$\mathrm{MA}_{0.8}\mathrm{Cs}_{0.2}$	I	-0.98	**0.63 ± 0.06**	1.63	0.992	0.77
$\mathrm{MA}_{0.8}\mathrm{FA}_{0.2}$	I	-0.93	**0.70 ± 0.02**	1.57	0.998	0.66
$\mathrm{MA}_{0.8}\mathrm{GA}_{0.2}$	I	-0.99	**0.94 ± 0.16**	1.61	0.890	0.53
MA	Br	-0.68	**0.49 ± 0.13**	2.35	0.877	0.70

Table S4. Crystal structure and lattice parameters for different $APbX_3$ end members.

***AMX*₃ composition**	**Crystal Structure**	**Lattice Parameters**		
		Tetragonal		**Pseudo-cubic**
		a = b (Å)	c (Å)	(Å)
$MAPbI_3$	Tetragonal	8.88	12.67	6.306
$MA_{0.8}Cs_{0.2}PbI_3$	Tetragonal	8.86	12.65	6.296
$MA_{0.8}GA_{0.2}PbI_3$	Tetragonal	8.95	12.95	6.400
$MA_{0.5}FA_{0.5}PbI_3$	(Pseudo)Cubic	-	-	6.338
$FA_{0.8}Cs_{0.2}PbI_3$	Tetragonal	8.95	12.71	6.340
$MAPbBr_3$	(Pseudo)Cubic	-	-	5.933

Table S5. Quadratic fit parameters for composition dependence of bandgap in $MAM(I_{1-z}Br_z)_3$ alloys.

Bowing (*b*) in $MAM(I_{1-z}Br_z)_3$ alloys obtained from quadratic fit of E_g data: $y = E_g(z) = az + bz^2 + c$					
A-site	*M*-site	a $(E_{Br} - E_I - b)$	***b*, eV**	c (E_I)	Adjusted R^2
MA	Pb	0.46	**0.26 ± 0.03**	1.57	0.999
MA	$Pb_{0.75}Sn_{0.25}$	0.52	**0.17 ± 0.05**	1.36	0.996
MA	Sn	0.65	**0.11 ± 0.05**	1.39	0.997

Table S6a. Molecular structure of different organic cations employed for synthesis of 2-dimensional (2D) mixed Pb-Sn perovskite alloys in literature.[13,14]

Organic Cation	**Notation**	**Structure**	**Ref.**
Benzylammonium	$(BZA)^+$	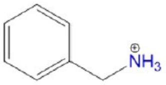	14
Benzimidazolium	$(Bn)^+$	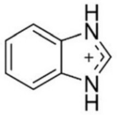	13
Histammonium	$(HA)^{2+}$	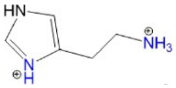	14

Table S6b. Structural and optical characteristics of 2D perovskite Sn-end members with organic cations employed for synthesis of mixed Pb-Sn perovskite alloys in literature.[13,14]

Composition	**Sn-I-Sn tilting angle (°)**	**E_g (eV)**	**Ref.**
$(BZA)_2SnI_4$	160.6	1.89	14
$(Bn)_2SnI_4$	173.9	1.81	13
$(HA)SnI_4$	160.0/178.5	1.67	14

Table S6c. Quadratic fit parameters for composition dependence of bandgap in 2D mixed Pb-Sn perovskite alloys.

Bowing (*b*) in $APb_{1-x}Sn_xI_4$ (2D) alloys obtained from quadratic fit of E_g data: $y = E_g(x) = ax + bx^2 + c$				
A-site	a ($E_{Sn} - E_{Pb} - b$)	***b*, eV**	c (E_{Pb})	Adjusted R^2
$(BZA)_2$	-1.14	**0.89 ± 0.25**	2.15	0.851
$(Bn)_2$	-0.86	**0.60 ± 0.15**	2.08	0.882
(HA)	-0.78	**0.46 ± 0.30**	2.02	0.775

Supplementary Figures

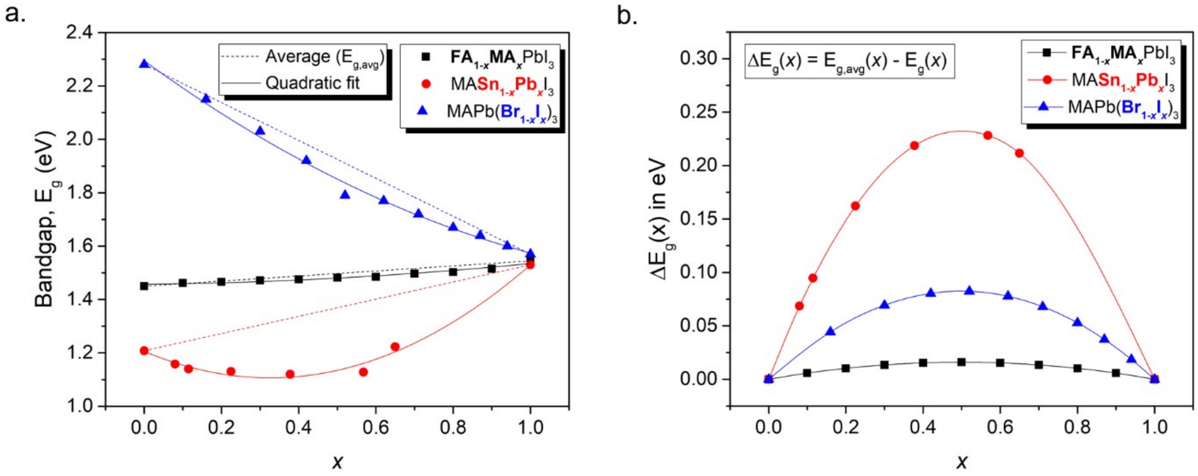

Figure S1. Bandgap variation in widely employed binary organic-inorganic hybrid perovskite (HP) alloys. (a) Bandgap (E_g) values for (MA,FA)PbI_3, MA(Pb,Sn)I_3 and MAPb(I,Br)$_3$ obtained from literature.[15–17] (b) Calculated differences in bandgap values (ΔE_g) between simple linear interpolation of end members ($E_{g,avg}$) and quadratic fit of the experimental data (E_g) shown in (a).

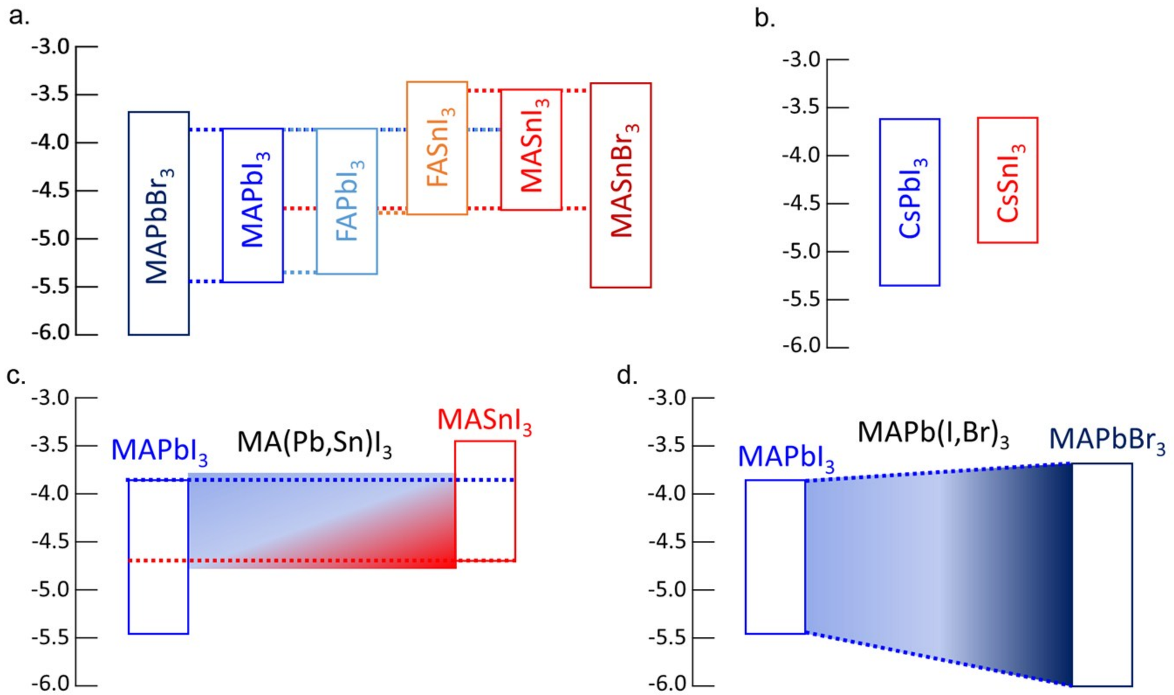

Figure S2. Frontier energy level variation as a function of composition in HPs. (a, b) Positions of valence band maximum (VBM) and conduction band minimum (CBM) for different Pb- and Sn-based HP compositions. VBM data for $MAPbI_3$,[18] $MASnI_3$,[18] $FAPbI_3$,[19] $FASnI_3$,[20] $MAPbBr_3$,[21] $MASnBr_3$,[22] $CsPbI_3$,[23] and $CsSnI_3$[24] were obtained from the associated references in literature; corresponding positions of CBM were calculated using the bandgap. (c, d) Schematic illustration for dependence of VBM and CBM characteristics on the nature of band offsets between end members in HP alloys; staggered (Type II) nature of band offset between $MAPbI_3$ and $MASnI_3$ results in the lowest bandgap at an intermediate alloy composition (c), whereas straddled (Type I) nature of band offset between $MAPbI_3$ and $MAPbBr_3$ results in the lowest bandgap at an end member composition (d).[25]

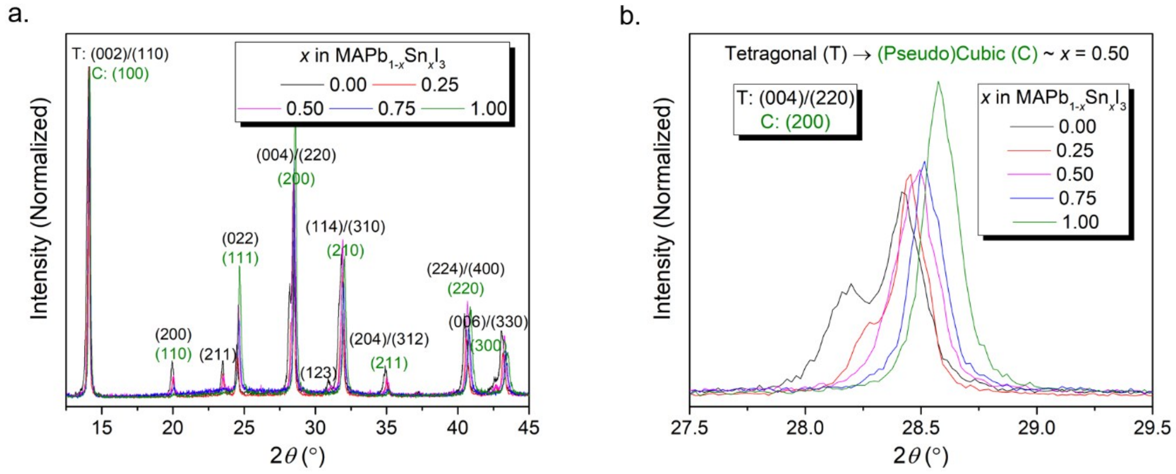

Figure S3. X-ray diffraction (XRD) measurements for powder samples of MAPb$_{1-x}$Sn$_x$I$_3$ alloys using a 1D detector. (a) XRD data with indexed peaks; indices in black color are for samples ($x < 0.50$) with tetragonal (T) structure and indices in green color are for samples ($x \geq 0.50$) with cubic (C) structure. (b) Zoomed-in T: (004)/(220) / C: (200) peak region from (a) to illustrate changes in peak position and transition from tetragonal to (pseudo)cubic structure ~ $x = 0.50$.

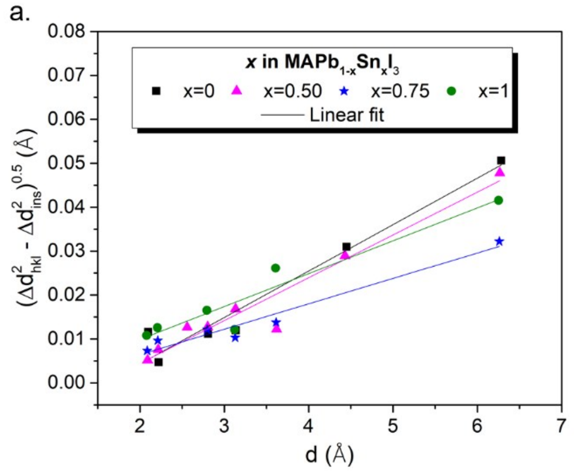

b.

x	Slope, ε	Standard Error	Adjusted R^2
0.00	0.0106	0.0011	0.945
0.50	0.0098	0.0010	0.933
0.75	0.0058	0.0006	0.947
1.00	0.0075	0.0011	0.900

Figure S4. Modified Williamson-Hall (W-H) plots for MAPb$_{1-x}$Sn$_x$I$_3$ alloys. (a) Plots of $(\Delta d_{hkl}^2 - \Delta d_{ins}^2)^{0.5}$ versus d along with linear fits of the data. (b) Linear fit parameters for fits in (a); slope represents microstrain (ε). Analysis method is described in the **Experimental Section**.

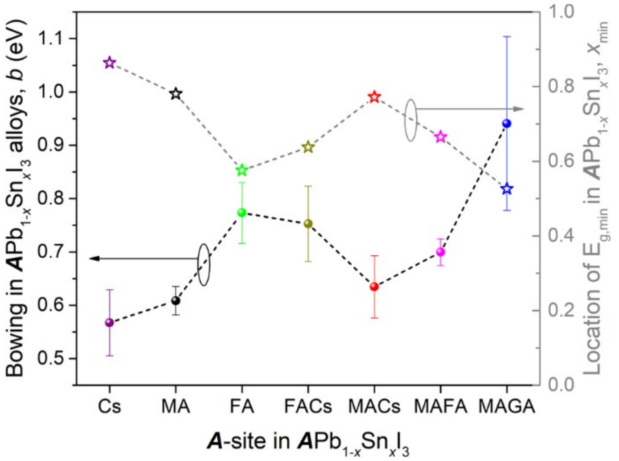

Figure S5. *A*-site dependence of bandgap bowing (b) and location of minimum bandgap ($x_{\min}$) in $A\mathrm{Pb}_{1-x}\mathrm{Sn}_x\mathrm{I}_3$ alloys.

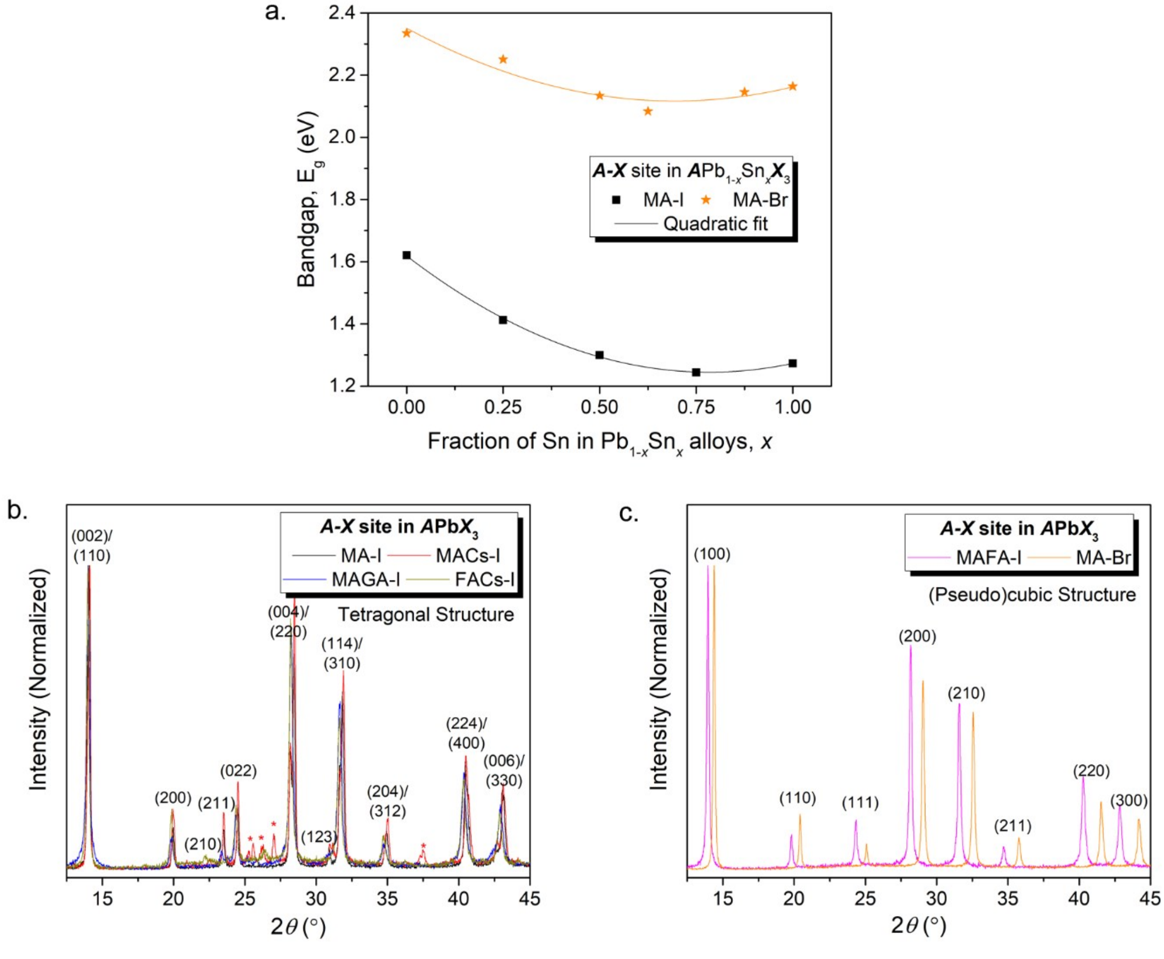

Figure S6. (a) Bandgap variation in $\mathrm{MAPb}_{1-x}\mathrm{Sn}_x\mathrm{Br}_3$ alloys in comparison to $\mathrm{MAPb}_{1-x}\mathrm{Sn}_x\mathrm{I}_3$ alloys. (b, c) XRD data (measurements for powder samples using a 1D detector) with indexed peaks for different $A\mathrm{Pb}X_3$ end member compositions; secondary impurity phases were observed only in MACs-I and are indicated by red asterisks.

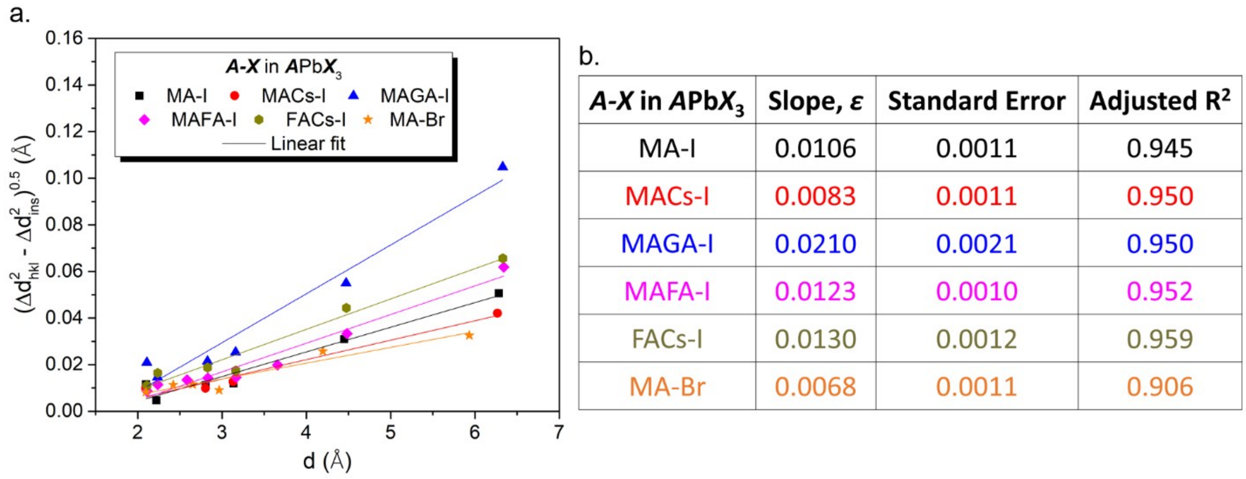

***A-X* in *A*Pb*X*$_3$**	**Slope, *ε***	**Standard Error**	**Adjusted R^2**
MA-I	0.0106	0.0011	0.945
MACs-I	0.0083	0.0011	0.950
MAGA-I	0.0210	0.0021	0.950
MAFA-I	0.0123	0.0010	0.952
FACs-I	0.0130	0.0012	0.959
MA-Br	0.0068	0.0011	0.906

Figure S7. Modified Williamson-Hall (W-H) plots for *A*Pb*X*$_3$ end members. (a) Plots of $(\Delta d_{hkl}^2 - \Delta d_{ins}^2)^{0.5}$ versus d along with linear fits of the data. (b) Linear fit parameters for fits in (a); slope represents microstrain (ε). Analysis method is described in the **Experimental Section**.

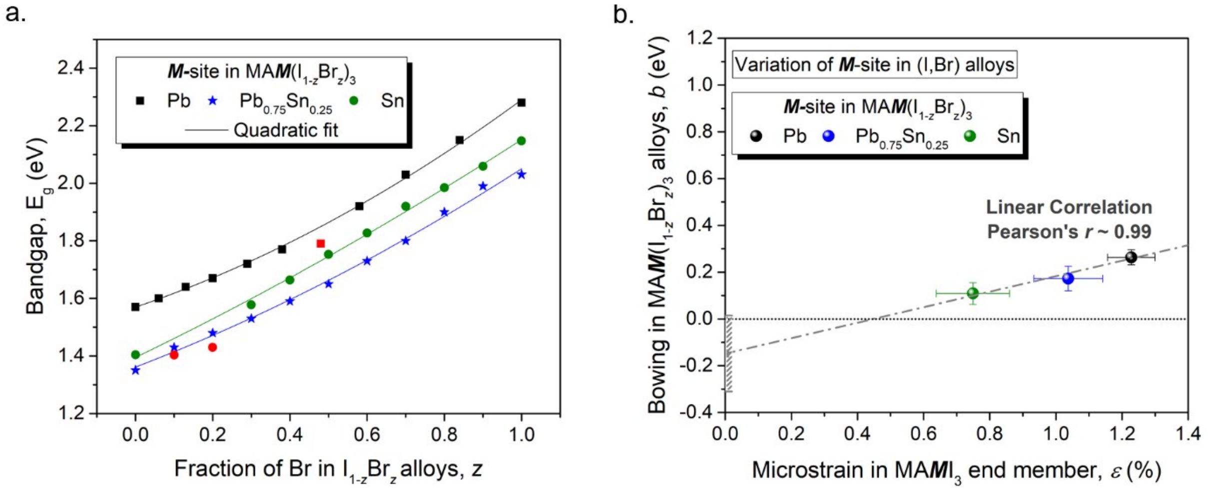

Figure S8. Bandgap variation in mixed halide (I-Br) HP alloys. (a) Bandgap data for different MA*M*$(I_{1-z}Br_z)_3$ alloy compositions along with quadratic fits; absorption onset data for MAPb$(I_{1-z}Br_z)_3$,[15] MA$Pb_{0.75}Sn_{0.25}(I_{1-z}Br_z)_3$,[26] and MASn$(I_{1-z}Br_z)_3$[27] were taken from the associated references in literature. Data points indicated in red color were considered as outliers and excluded from fitting. (b) Plot of bandgap bowing in MA*M*$(I_{1-z}Br_z)_3$ alloys versus microstrain in their respective MA*M*I_3 end members (variation of *M*-site in I/Br alloys); a linear correlation with Pearson correlation coefficient (*r*) ~ 0.99 is observed.

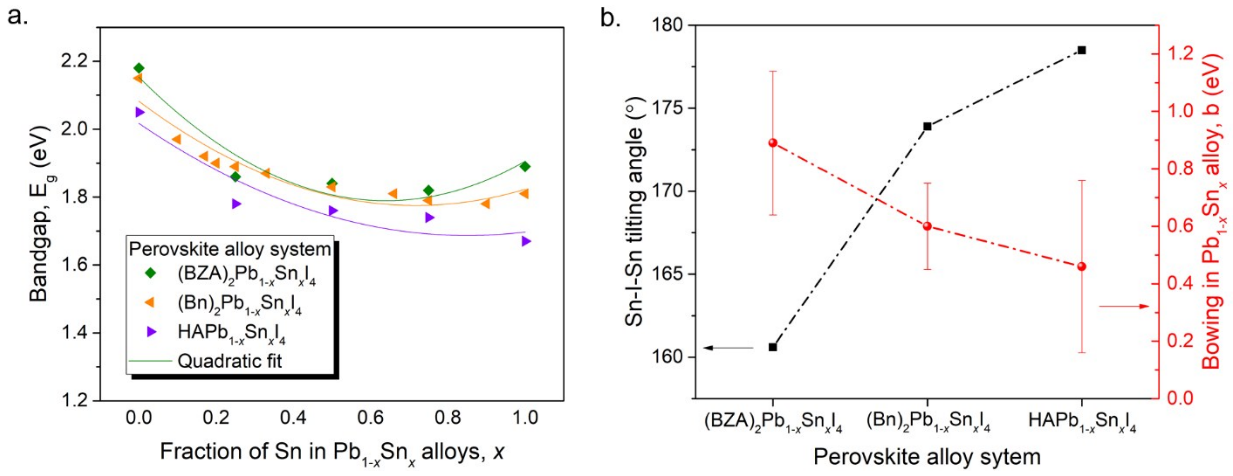

Figure S9. (a) Bandgap data for various mixed Pb-Sn 2D perovskite alloy systems with different fractions of Sn; data for $(BZA)_2Pb_{1-x}Sn_xI_4$,[14] $(Bn)_2Pb_{1-x}Sn_xI_4$,[13] and $HAPb_{1-x}Sn_xI_4$[14] were taken from the associated references in literature. (b) Variations in bandgap bowing for different mixed Pb-Sn 2D perovskite alloy systems and Sn-I-Sn tilting angle in their respective Sn-end members.

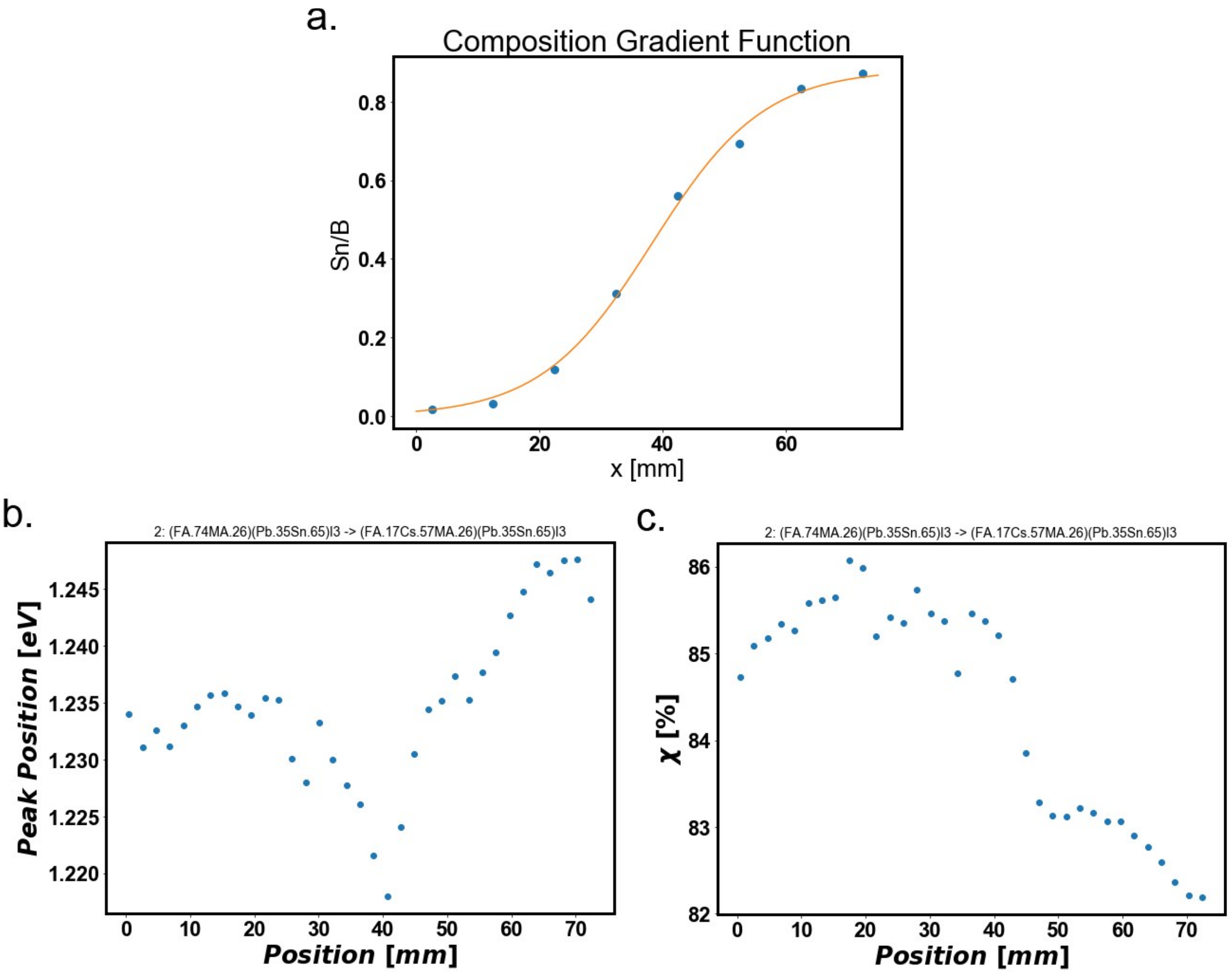

Figure S10. (a) EDS data demonstrating the changing composition as a function of distance along the 75 mm substrate. For this validation gradient, we used a pure Pb to a pure Sn composition, $(FA_{0.75}Cs_{0.25})PbI_3$ to $(FA_{0.75}Cs_{0.25})SnI_3$, since Pb and Sn are easy to differentiate with EDS. (b) example PL peak position and (c) example optoelectronic quality χ ($\chi \equiv \Delta E_F/V_{OC,SQ}$) for a single composition gradient, where the composition changes from $(FA_{0.74}MA_{0.26})(Pb_{0.35}Sn_{0.65})I_3$ at 0 mm to $(FA_{0.17}Cs_{.57}MA_{0.26})(Pb_{0.35}Sn_{0.65})I_3$ at 75mm according to the gradient function shown in (a).

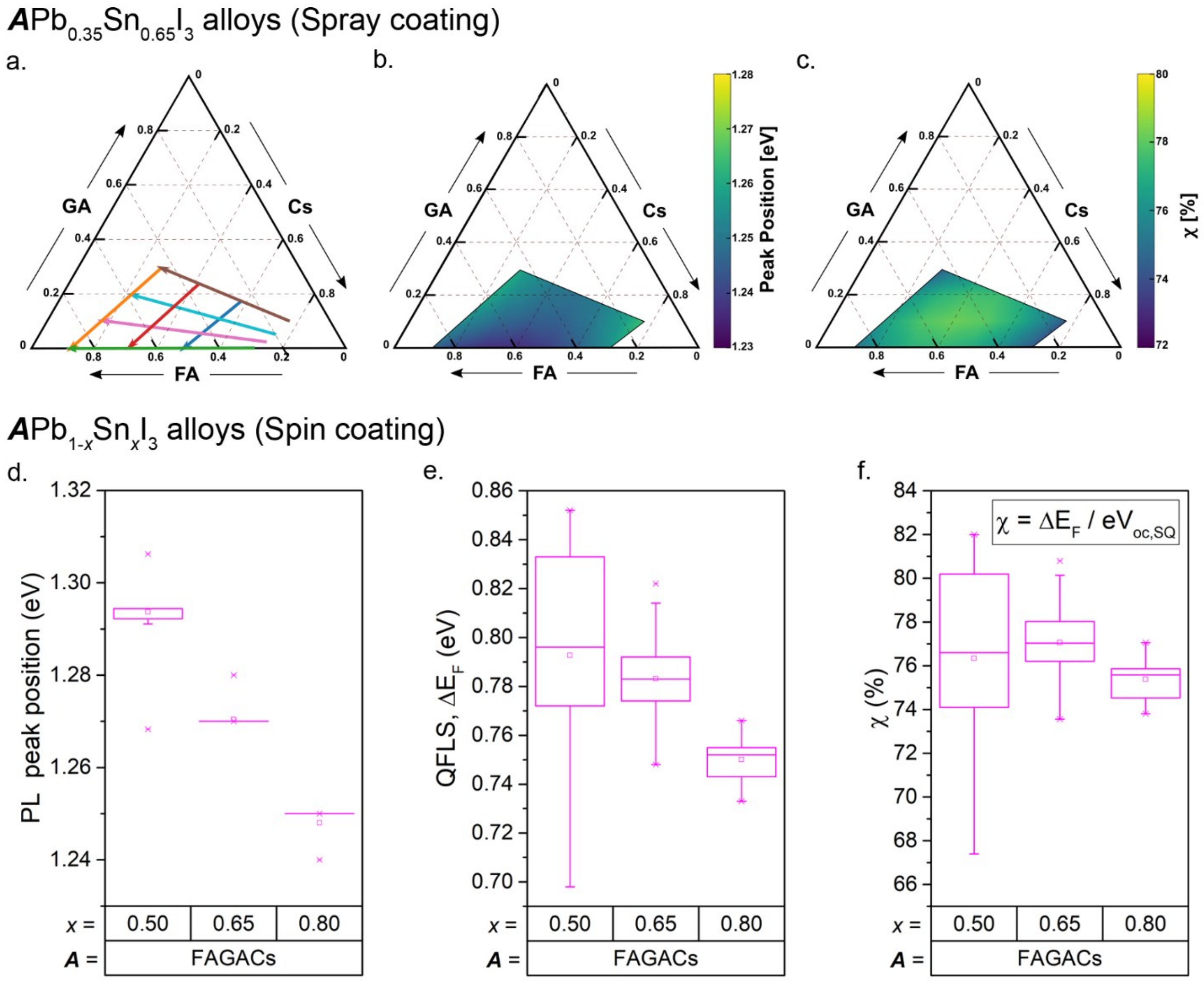

Figure S11. (a-c) Spray coating results for FAGACs films. (a) The seven gradients used to explore the FAGACs composition space (each color represents one gradient). Compositions were chosen to keep effective tolerance factor between 0.92 and 1.00. (b) PL peak position for (FA,GA,Cs) dataset. (c) Optoelectronic quality χ ($\chi \equiv \Delta E_F/V_{OC,SQ}$) for the (FA,GA,Cs) dataset. (d-f) PL results on FAGACs spin coated films, where A = $FA_{0.42}Cs_{0.45}GA_{0.12}$ and x = Sn/Pb+Sn = 0.50, 0.65, or 0.80.

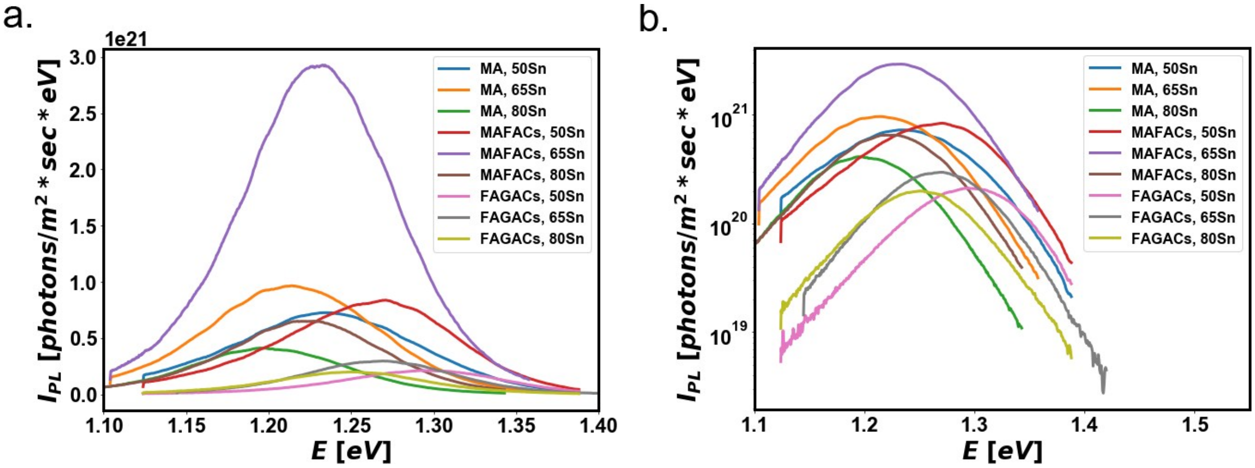

Figure S12. Absolute intensity Photoluminescence spectra for spin coated films with three different *A*-site and *B*-site compositions, plot on a linear (a) and log (b) axis. MAFACs represent *A* = $MA_{0.24}FA_{0.61}Cs_{0.15}$, and FAGACs represents *A* = $FA_{0.42}Cs_{0.45}GA_{0.12}$. 50Sn, 65Sn, and 80Sn correspond to *B*-site composition of *x* = Sn/Pb+Sn = 0.50, 0.65, and 0.80, respectively.

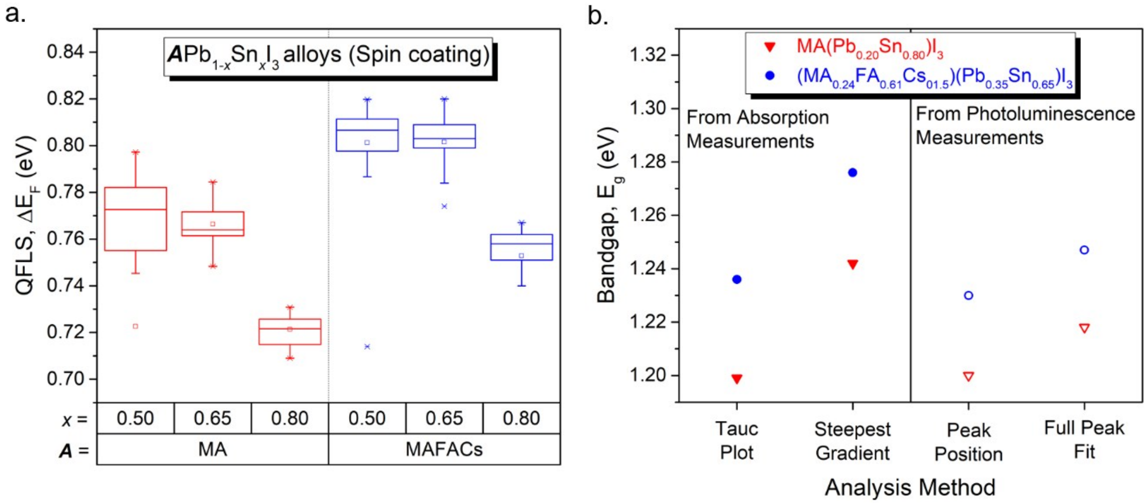

Figure S13. (a) Quasi-Fermi Level splitting of MA and MAFACs spin coated films with *x* = Sn/Pb+Sn = 0.50, 0.65, and 0.80. MAFACs represent *A* = $MA_{0.24}FA_{0.61}Cs_{0.15}$. (b) Bandgap of $[(MA)(Pb_{0.20}Sn_{0.30})I_3]$ and $[(MA_{0.24}FA_{0.61}Cs_{0.15})(Pb_{0.35}Sn_{0.65})I_3]$ determined using different analysis methods: Tauc plot and steepest gradient methods were used to obtain bandgap from absorption (UV-vis) measurements; Peak position and full peak fit of the PL spectra were used to obtain bandgap from photoluminescence (AIPL) measurements. Details of different analysis methods are provided in **Experimental Section**.

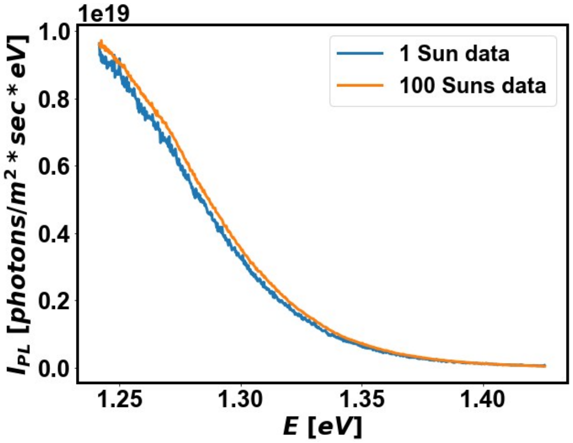

Figure S14. Comparison of PL emission of a typical MAFACs spin coated film measured at 1 Suns and measured at 100 Suns with 1 Sun correction. The 100 Suns data was corrected to 1 Sun by multiplying by dividing the spectrum by N-Suns, where N-Suns is the precise ratio of incident laser photon flux divided by 1 Sun above bandgap photon flux at AM 1.5. Since 1 Sun data and 100 Sun corrected data give exactly the same emission flux, we conclude that PLQY is similar at 1 Sun and 100 Suns and can appropriately use 100 Sun data in our 1 Sun quasi-Fermi Level splitting corrections. The data above was collected with Si detector, which has low responsivity below 1.25eV, while the InGaAs detector has high background. Thus using 100 Sun data collected with InGaAs detector is the most appropriate method to quality AIPL data in this study.

REFERENCES

(1) Parrott, E. S.; Green, T.; Milot, R. L.; Johnston, M. B.; Snaith, H. J.; Herz, L. M. *Adv. Funct. Mater.* **2018**, *28* (33), 1802803.

(2) Rajagopal, A.; Stoddard, R. J.; Jo, S. B.; Hillhouse, H. W.; Jen, A. K.-Y. *Nano Lett.* **2018**, *18* (6), 3985–3993.

(3) Stoddard, R. J.; Rajagopal, A.; Palmer, R. L.; Braly, I. L.; Jen, A. K.-Y.; Hillhouse, H. W. *ACS Energy Lett.* **2018**, *3* (6), 1261–1268.

(4) Williams, S. T.; Rajagopal, A.; Jo, S. B.; Chueh, C.-C.; Tang, T. F. L.; Kraeger, A.; Jen, A. K.-Y. *J. Mater. Chem. A* **2017**, *5* (21), 10640–10650.

(5) Eperon, G. E.; Stranks, S. D.; Menelaou, C.; Johnston, M. B.; Herz, L. M.; Snaith, H. J. *Energy Environ. Sci.* **2014**, *7* (3), 982.

(6) Zhao, Y.; Zhang, J. *J. Appl. Crystallogr.* **2008**, *41* (6), 1095–1108.

(7) Wang, J. T.-W.; Wang, Z.; Pathak, S.; Zhang, W.; DeQuilettes, D. W.; Wisnivesky-Rocca-Rivarola, F.; Huang, J.; Nayak, P. K.; Patel, J. B.; Mohd Yusof, H. A.; Vaynzof, Y.; Zhu, R.; Ramirez, I.; Zhang, J.; Ducati, C.; Grovenor, C.; Johnston, M. B.; Ginger, D. S.; Nicholas, R. J.; Snaith, H. J. *Energy Environ. Sci.* **2016**, *9* (9), 2892–2901.

(8) Hoke, E. T.; Slotcavage, D. J.; Dohner, E. R.; Bowring, A. R.; Karunadasa, H. I.; McGehee, M. D. *Chem. Sci.* **2015**, *6* (1), 613–617.

(9) Kim, D.; Yun, J. S.; Sharma, P.; Lee, D. S.; Kim, J.; Soufiani, A. M.; Huang, S.; Green, M. A.; Ho-Baillie, A. W. Y.; Seidel, J. *Nat. Commun.* **2019**, *10* (1), 444.

(10) Braly, I. L.; Hillhouse, H. W. *J. Phys. Chem. C* **2016**, *120* (2), 893–902.

(11) Ross, R. T. *J. Chem. Phys.* **1967**, *46* (12), 4590–4593.

(12) Katahara, J. K.; Hillhouse, H. W. *J. Appl. Phys.* **2014**, *173504*.

(13) Zimmermann, I.; Aghazada, S.; Nazeeruddin, M. K. *Angew. Chemie Int. Ed.* **2019**, *58* (4), 1072–1076.

(14) Mao, L.; Tsai, H.; Nie, W.; Ma, L.; Im, J.; Stoumpos, C. C.; Malliakas, C. D.; Hao, F.; Wasielewski, M. R.; Mohite, A. D.; Kanatzidis, M. G. *Chem. Mater.* **2016**, *28* (21), 7781–7792.

(15) Noh, J. H.; Im, S. H.; Heo, J. H.; Mandal, T. N.; Seok, S. Il. *Nano Lett.* **2013**, *13* (4), 1764–1769.

(16) Im, J.; Stoumpos, C. C.; Jin, H.; Freeman, A. J.; Kanatzidis, M. G. *J. Phys. Chem. Lett.* **2015**, *6* (17), 3503–3509.

(17) Weber, O. J.; Charles, B.; Weller, M. T. *J. Mater. Chem. A* **2016**, *4* (40), 15375–15382.

(18) Yang, Z.; Rajagopal, A.; Chueh, C.; Jo, S. B.; Liu, B.; Zhao, T.; Jen, A. K.-Y. *Adv. Mater.* **2016**, *28* (40), 8990–8997.

(19) Lee, J.-W.; Seol, D.-J.; Cho, A.-N.; Park, N.-G. *Adv. Mater.* **2014**, *26* (29), 4991–4998.

(20) Ke, W.; Stoumpos, C. C.; Logsdon, J. L.; Wasielewski, M. R.; Yan, Y.; Fang, G.; Kanatzidis, M. G. *J. Am. Chem. Soc.* **2016**, *138* (45), 14998–15003.

(21) Endres, J.; Egger, D. A.; Kulbak, M.; Kerner, R. A.; Zhao, L.; Silver, S. H.; Hodes, G.; Rand, B. P.; Cahen, D.; Kronik, L.; Kahn, A. *J. Phys. Chem. Lett.* **2016**, *7*, 2722–2729.

(22) Hao, F.; Stoumpos, C. C.; Cao, D. H.; Chang, R. P. H.; Kanatzidis, M. G. *Nat. Photonics* **2014**, *8* (6), 489–494.

(23) Li, B.; Zhang, Y.; Zhang, L.; Yin, L. *Adv. Mater.* **2017**, *29* (39), 1701221.

(24) Wang, N.; Zhou, Y.; Ju, M.-G.; Garces, H. F.; Ding, T.; Pang, S.; Zeng, X. C.; Padture, N. P.; Sun, X. W. *Adv. Energy Mater.* **2016**, *6* (24), 1601130.

(25) Goyal, A.; McKechnie, S.; Pashov, D.; Tumas, W.; Schilfgaarde, M. Van; Stevanović, V.

Chem. Mater. **2018**, *30* (11), 3920–3928.

(26) Yang, Z.; Rajagopal, A.; Jo, S. B.; Chueh, C.-C.; Williams, S.; Huang, C.-C.; Katahara, J. K.; Hillhouse, H. W.; Jen, A. K.-Y. *Nano Lett.* **2016**, *16* (12), 7739–7747.

(27) Lai, M. L.; Tay, T. Y. S.; Sadhanala, A.; Dutton, S. E.; Li, G.; Friend, R. H.; Tan, Z.-K. *J. Phys. Chem. Lett.* **2016**, *7* (14), 2653–2658.